A novel approach for state of charge estimation based on adaptive switching gain sliding mode observer in electric vehicles

Xiaopeng Chen, Weixiang Shen*, Zhenwei Cao, Ajay Kapoor

Faculty of Engineering and Industrial Sciences, Swinburne University of Technology, Hawthorn, Victoria 3122, Australia

HIGHLIGHTS

- State equations are derived from the battery equivalent circuit model.
- An adaptive switching gain sliding mode observer for state of charge estimation is purposed.
- The new observer minimises the chattering and improves the estimation accuracy.
- The experimental results of a lithium-polymer battery verify the effectiveness of the purposed observer.

ARTICLE INFO

ABSTRACT

In this paper, a novel approach for battery state of charge (SOC) estimation in electric vehicles (EVs) based on an adaptive switching gain sliding mode observer (ASGSMO) has been presented. To design the ASGSMO for the SOC estimation, the state equations based on a battery equivalent circuit model (BECM) are derived to represent dynamic behaviours of a battery. Comparing with a conventional sliding mode observer, the ASGSMO has a capability of minimising chattering levels in the SOC estimation by using the self-adjusted switching gain while maintaining the characteristics of being able to compensate modelling errors caused by the parameter variations of the BECM. Lyapunov stability theory is adopted to prove the error convergence of the ASGSMO for the SOC estimation. The lithium-polymer battery (LiPB) is utilised to conduct experiments for determining the parameters of the BECM and verifying the effectiveness of the proposed ASGSMO in various discharge current profiles including EV driving conditions in both city and suburban.

1. Introduction

Due to the progressive rise of petrol costs and environmental concerns on exhaust emission from petrol-driven vehicles, the eco-friendly electric vehicles (EVs) have greatly exhibited promising potential to revive as the leading means of transportation in up-coming decades. The EV performance is highly dependent on battery characteristics such as operation voltage, temperature, charge or discharge rate and aging. Among existing battery types applicable to EVs, lithium-polymer battery (LiPB) is widely recognised as the most capable candidate for the development and innovation of the new generation EVs. Compared with other types of EV batteries such as lead-acid batteries, nickel–cadmium batteries and nickel–metal hydride batteries, LiPBs are superior in terms of high energy and power density, broad operating temperature range, rapid charge capability, no memory effects, long cycle life and extremely low self-discharge rate [1,2].

The amount of battery available capacity is closely related to the state of charge (SOC), which is considered as one of the key factors in battery management system (BMS) for supporting optimal battery performance and safety in EVs. The accurate battery SOC indication is essential for predicting a reliable travelling range, maximising the efficiency of battery energy utilisation and preventing the batteries in EVs from over-charging or over-discharging. Unfortunately, the SOC involves in intrinsic electrochemical processes of a battery, and it cannot be directly measured by a sensor. It should be estimated by an advanced mathematical algorithm with the aids of measurable signals such as terminal voltage and current from the battery.

* Corresponding author. Tel.: +61 3 9214 5886; fax: +61 3 9214 8264.
E-mail addresses: xchen@swin.edu.au, wshen@swin.edu.au (W. Shen).

A number of techniques have been proposed to estimate the SOC of a battery and each one has its own advantages in certain aspects [3–5]. The most straightforward approach is the ampere-hour (Ah) counting, which simply integrates the battery charge and discharge currents over time. The SOC can be calculated by referring to the calibration point at the fully charged battery. This method is inexpensive to be implemented in hardware, but the estimation accuracy is strongly dependent on the sampling frequency and the precision of the current sensor. Moreover, this non-model and open-loop-based estimator can easily accumulate errors caused by embedded noises and current measurement drift and it is also incapable of determining the initial SOC. An enhanced version of Ah counting has shown improved SOC estimation results by online evaluating Coulombic efficiency with recalibration of the battery capacity [6].

The impedance measurement has been declared as an effective technique for the SOC estimation [7–9]. It loads a series of small amplitude a.c. signals into a battery to detect the responses of the battery in the wide range of frequencies. The SOC can be obtained by analysing the battery impedance, but the measured impedances cannot completely represent the dynamics of batteries in the case of large discharge current in EVs. Another drawback of this approach is that a set of the bulky and costly auxiliary equipment such as the signal generator and the impedance spectroscope is required to carry out impedance measurement.

Another category of the SOC estimation methods is relied on computational and intelligence-based strategies, which encompass artificial neural networks (NNs), fuzzy neural networks, adaptive fuzzy neural networks and support vector machine [10–13]. These data-oriented approaches can accurately estimate the SOC for all kinds of batteries in the absence of the details of batteries, but they require a large number of training sample data to train the NNs. Therefore, they demand more powerful and costly data processing chips to handle the massive computation loads in the BMSs. Furthermore, the SOC would be unpredictable in case of discharge current profiles loaded in EV batteries deviated from those represented by the training data.

The Kalman filter (KF), as a classical state estimation method for dynamic systems, was also developed to estimate the SOC based on a linear model [14,15]. For the battery represented by a nonlinear model, some advanced KF techniques such as extended KF (EKF) [16,17], sigma-point KF (SPKF) [18,19] and unscented KF (UKF) [20,21] were proposed to achieve online SOC estimation. The essential idea of the EKF approach is to transform a nonlinear system into a linear system by linearising the nonlinear function based on the first order Taylor series expansion, such a process gives rise to large linearisation errors and complicated computation of the Jacobian matrix which may lead to the instability of the filter and inaccurate estimation for highly nonlinear battery systems in EVs. Instead of the local linearisation in the EKF, the SPKF and UKF approaches use an unscented transformation to approximate a Gaussian distribution of the state random variable with a set of sample points or sigma points and offer better SOC estimation results in terms of accuracy and robustness [18–21].

All these KF-based SOC estimation algorithms, however, require accurate battery model parameters with the assumption that constant values of the process and measurement noise covariance are priori known, which are hardly practical and error-prone due to the complex electrochemical reactions inside batteries for EV driving conditions. Furthermore, the constant values of noise covariance can result in remarkable errors and divergence in the battery SOC estimation. Later, both an adaptive EKF (AEKF) and an adaptive UKF (AUKF) have been developed to estimate the values of the process and measurement noise covariance during the online process [22,23]. They have demonstrated better precision in the SOC estimation and filter divergence restraint at the expense of higher complexity and computational cost.

More recently, the H_∞ observer-based method has been proposed to estimate the SOC without the requirement of the exact statistical properties of the battery. This method minimises the errors of system and measurement so that the SOC estimation error is less than a given attenuation level [24,25], where an alternative feedback gain is employed to tackle modelling errors and disturbances. Similarly, the sliding mode observer (SMO) based SOC estimation method has been adopted to overcome the uncertainties of battery model, external disturbances and measurement noises [26,27]. Nevertheless, this method relies on the exhaustive understanding of battery dynamics for the appropriate selection of the SMO parameters such as uncertainty boundaries and switching gains, leading to the trade-off between the chattering magnitude and the convergence speed in the SOC estimation.

In this paper, a novel approach for the SOC estimation based on an adaptive switching gain sliding mode observer (ASGSMO) has been proposed. Comparing with constant switching gains SMO, the ASGSMO is able to dynamically adjust the switching gains in response to the tracking errors, and guarantee the reachability of sliding mode surface and trigger the sliding mode. Once the sliding mode is activated, the switching gains are self-tuned to "adequate" levels to counteract the modelling errors and reduce the chattering magnitudes, thereby improving the SOC estimation accuracy.

The remaining part of this paper is organised as follows. In Section 2, a battery equivalent circuit model (BECM) is presented to characterise the discharge behaviours of the LiPB in the presence of parameter uncertainties. The detailed procedures to identify the BECM parameters are also explained in this section. In Section 3, the ASGSMO design methodology is elaborated for the SOC estimation. The proposed ASGSMO is validated for SOC estimation by experimental results in Section 4, followed by conclusions in Section 5.

2. Battery modelling

2.1. Battery equivalent circuit model

There have been numerous attempts to establish a precise battery model for achieving an accurate battery state estimation. The battery equivalent circuit models consisting of circuit components such as capacitors, resistors, diodes and voltage sources have been widely studied and developed to capture dynamic characteristics of a battery for reducing modelling errors [28–30]. These circuit-based models are also applied to the battery SOC estimation due to their state equations are intuitively derived from circuit analysis for mathematical computation. In this paper, without the
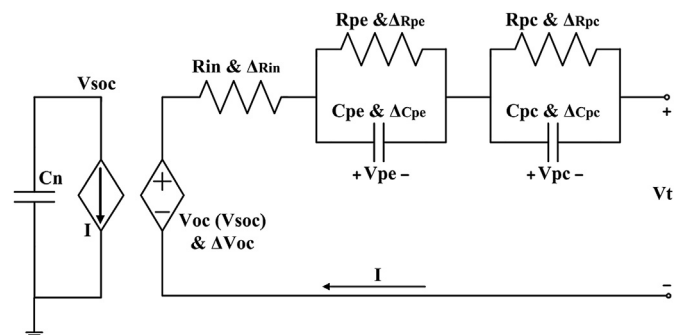

Fig. 1. Schematic diagram of BECM.

consideration of a hysteresis effect, a BECM is used to model the LiPB dynamics and its schematic diagram is shown in Fig. 1, where the variations of the circuit parameters are also included to represent the modelling errors.

In the BECM, a capacitor C_n with the nominal capacity represents the total stored energy in the battery. V_t and I represent the battery terminal voltage and discharge current, respectively. The voltage across C_n as V_{soc} varies in the range of the SOC from 0% (the fully discharged) to 100% (the fully charged), and it represents the SOC quantitatively. A voltage-controlled current source I (V_{soc}) and voltage-controlled voltage source V_{oc} (V_{soc}) are used to bridge a nonlinear relationship between the SOC (i.e., V_{soc}) and the open circuit voltage (OCV) of the LiPB as shown in Fig. 2, which can be derived by fitting the experimental data from a pulse current discharge (PCD) profile (see details later).

Two parallel resistive and capacitive branches consist of the electrochemical polarisation resistance R_{pe}, capacitance C_{pe}, the concentration polarisation resistance R_{pc} and capacitance C_{pc}, which reflect the short-term and long-term transient responses due to the relaxation effect of battery, respectively. This relaxation effect represents the slow convergence of battery terminal voltage to the OCV (V_{oc}) at its equilibrium state after several hours of relaxation at the end of charging or discharging. It is mostly caused by a diffusion effect and a double-layer charging or discharging effect in the battery [28]. An ohmic resistor R_{in} characterises the charging or discharging energy losses of battery. The self-discharge resistance is neglected in this model as the LiPB has extremely low self-discharge rate.

The symbols ΔV_{oc}, ΔR_{in}, ΔR_{pe}, ΔC_{pe}, ΔR_{pc} and ΔC_{pc} associated with corresponding circuit components represent variations of the circuit parameters caused by the combination of modelling errors and disturbances. There are two main causes for modelling errors. Firstly, the circuit parameters of the BECM are determined as the constant values, but in fact they are varying with the battery SOC and temperature in different discharge current profiles. Secondly, the nonlinear relationship of OCV−SOC curve is piecewise linearised as derived later and it results in large linearisation errors.

The SOC is a value between 0% and 100% that indicates the ratio of available capacity to the nominal capacity in the battery. It can be obtained through the Ah counting approach by taking a time integral of measured battery current as expressed by Eq. (1).
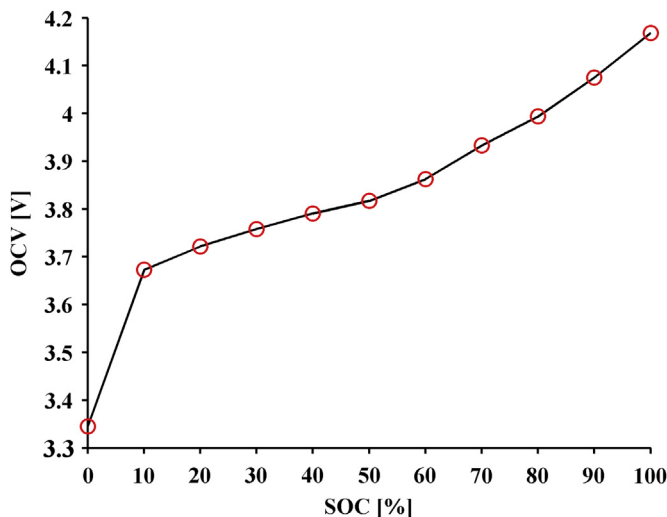
$$Soc(t_1) = Soc(t_0) - (1/C_n) \int_{t_0}^{t_1} \eta I(\tau) d\tau \tag{1}$$

where $Soc(t_0)$ denotes the initial SOC, C_n is the battery nominal capacity in ampere-hours, $I(\tau)$ is the instantaneous discharge current (assumed to be positive), and η is the Coulombic efficiency, which is usually taken as 1 for discharging and smaller than or close to 1 for charging for the LiPBs in the wide range of current and temperature.

According to the Kirchhoff voltage law in circuit theory, the battery terminal voltage V_t can be determined by Eq. (2).

$$V_t = V_{oc}(Soc) - V_{pe} - V_{pc} - IR_{in} + \Delta_{uncertain} \tag{2}$$

The time derivatives of SOC and polarisation voltages give

$$\dot{Soc} = -(I/C_n) + \Delta f_2 \tag{3}$$

$$\dot{V}_{pe} = -V_{pe}/(R_{pe}C_{pe}) + I/C_{pe} + \Delta f_3 \tag{4}$$

$$\dot{V}_{pc} = -V_{pc}/(R_{pc}C_{pc}) + I/C_{pc} + \Delta f_4 \tag{5}$$

where V_{pe} and V_{pc} denote the electrochemical and concentration polarisation voltages across C_{pe} and C_{pc}, respectively. The terms $\Delta_{uncertain}$, Δf_2, Δf_3 and Δf_4 not only represent model uncertainties caused by modelling errors, but also time-varying internal and external disturbances.

Despite the nonlinearity of OCV−SOC curve as shown in Fig. 2, there exists a piecewise linear relationship between the OCV and the SOC in a certain range of SOC indicated by the red dots in the curve. Therefore, the OCV can be expressed as a function of the SOC by using piecewise linearisation method.

$$V_{oc}(Soc) = \kappa Soc + \nu \tag{6}$$

where the values of κ and ν are varying in different SOC ranges.

Due to the fast sampling rate [27], the changing rate of discharge current I can be negligible, namely $dI/dt = 0$, the time derivative of terminal voltage V_t in Eq. (2) with the substitutions of Eqs. (3)–(6) gives

$$\dot{V}_t = -\kappa(I/C_n) + V_{pe}/(R_{pe}C_{pe}) - I/C_{pe} + V_{pc}/(R_{pc}C_{pc}) - I/C_{pc} + \Delta f_1 \tag{7}$$

Solving I in Eq. (2) and substituting it into Eq. (3) as well as re-arranging Eqs. (3)–(6) result in the state-space equations of the BECM as follows

$$\begin{aligned}
\dot{V}_t &= -a_1 V_t + a_1 V_{oc}(Soc) - a_3 V_{pe} - a_4 V_{pc} - b_1 I + \Delta f_1 \\
\dot{Soc} &= a_2 V_t - a_2 V_{oc}(Soc) + a_2 V_{pe} + a_2 V_{pc} + \Delta f_2 \\
\dot{V}_{pe} &= -a_4 V_{pe} + b_2 I + \Delta f_3 \\
\dot{V}_{pc} &= -a_3 V_{pc} + b_3 I + \Delta f_4
\end{aligned} \tag{8}$$

where $a_1 = 1/(R_{pe}C_{pe}) + 1/(R_{pc}C_{pc})$, $a_2 = 1/(R_{in}C_n)$, $a_3 = 1/(R_{pc}C_{pc})$, $a_4 = 1/(R_{pe}C_{pe})$, $b_1 = \kappa/C_n + R_{in}/(R_{pe}C_{pe}) + 1/C_{pe} + R_{in}/(R_{pc}C_{pc}) + 1/C_{pc}$, $b_2 = 1/C_{pe}$ and $b_3 = 1/C_{pc}$.

If the input and the output of circuit model are defined as $u(t) = I$ and $y(t) = V_t$, respectively, and the system state variables are chosen as V_t, $V_{oc}(Soc)$, V_{pe} and V_{pc}, then Eq. (8) of the BECM can be concisely expressed in matrices

$$\dot{x}(t) = Ax(t) + Bu(t) + \Delta f(x, u, t) \tag{9}$$

Fig. 2. Experimental OCV−SOC relationship of LiPB.

$$y(t) = Cx(t) \tag{10}$$

where

$$A = \begin{bmatrix} -a_1 & a_1 & -a_3 & -a_4 \\ a_2 & -a_2 & a_2 & a_2 \\ 0 & 0 & -a_4 & 0 \\ 0 & 0 & 0 & -a_3 \end{bmatrix}, \; B = \begin{bmatrix} -b_1 \\ 0 \\ b_2 \\ b_3 \end{bmatrix},$$

$C = [1 \quad 0 \quad 0 \quad 0]$ and $x(t) = [V_t V_{oc}(Soc) V_{pe} V_{pc}]^T$.

The unknown function $\Delta f(x,u,t)$ represents the matched model uncertainties and it can be assumed that

$$\Delta f(x, u, t) = \Gamma \xi(x, t) \tag{11}$$

where Γ is the model uncertainties input matrix and the function $\xi(x,t)$ is unknown but bounded

$$|\xi(x,t)| \le \psi \quad \forall x \in R^4, \; t \ge 0 \tag{12}$$

where the bound ψ is a positive constant and can be determined by the largest modelling errors between the experimental data and the BECM of the LiPB. According to Eq. (11), Eq. (9) is rewritten as

$$\dot{x}(t) = Ax(t) + Bu(t) + \Gamma \xi(x, t) \tag{13}$$

The success of applying the ASGSMO to estimate the internal states of the battery depends on the stability and observability of the corresponding linear parts of the BECM.

Remark 1:. The eigenvalues of the BECM system are obtained by

$$\det(\lambda I_0 - A) = \det \begin{bmatrix} \lambda + a_1 & a_1 & -a_3 & -a_4 \\ a_2 & \lambda + a_2 & a_2 & a_2 \\ 0 & 0 & \lambda + a_4 & 0 \\ 0 & 0 & 0 & \lambda + a_3 \end{bmatrix} = 0 \tag{14}$$

where I_0 is an identity matrix with appropriate dimensions. The eigenvalues of the matrix A are $\lambda_1 = -1/(R_{pe}C_{pe}) - 1/(R_{pc}C_{pc})$, $\lambda_2 = 0$, $\lambda_3 = -1/(R_{pe}C_{pe})$ and $\lambda_4 = -1/(R_{pc}C_{pc})$. Therefore, based on the modern control theory, the BECM system is stable.

Remark 2:. The observability matrix of the BECM system is

$$O_b(A, C) = \begin{bmatrix} C \\ CA \\ CA^2 \\ CA^3 \end{bmatrix} = \begin{bmatrix} 1 & 0 & 0 & 0 \\ -a_1 & a_1 & -a_3 & -a_4 \\ O_b(3,1) & O_b(3,2) & O_b(3,3) & O_b(3,4) \\ O_b(4,1) & O_b(4,2) & O_b(4,3) & O_b(4,4) \end{bmatrix} \tag{15}$$

where

$O_b(3, 1) = a_1^2 + a_2 a_1$, $O_b(3, 2) = -a_1^2 - a_2 a_1$,

$O_b(3, 3) = a_3 a_1 + a_2 a_1 + a_3 a_4$,

$O_b(3, 4) = a_4 a_1 + a_2 a_1 + a_3 a_4$,

$O_b(4, 1) = -a_1^3 - 2a_2 a_1^2 - a_2^2 a_1$,

$O_b(4, 2) = a_1^3 + 2a_2 a_1^2 + a_2^2 a_1$,

$O_b(4,3) = -a_3 a_1^2 - a_2 a_3 a_1 - a_2 a_1^2 - a_2^2 a_1 - a_4 a_3 a_1 - a_2 a_4 a_1 - a_4^2 a_3$,

$O_b(4,4) = -a_4 a_1^2 - a_2 a_4 a_1 - a_2 a_1^2 - a_2^2 a_1 - a_4 a_3 a_1 - a_2 a_3 a_1 - a_3^2 a_4$.

On the conditions of $1/(R_{pe}C_{pe}) \ne 1$, $1/(R_{pc}C_{pc}) \ne 1$ and $1/(R_{in}C_n) \ne 1$, which are always satisfied for the battery in normal operating conditions, then it enables the full rank of Eq. (15) so that the BECM system is observable and thus the internal states of the battery can be estimated by an observer.

The advantages of this BECM are that it relatively captures the dynamic behaviours of a LiPB with reasonable computational cost. Additionally, the modelling errors and disturbances also can be compensated by the robust ASGSMO.

2.2. Battery model parameters determination

The circuit parameters of the BECM in Fig. 1 are obtained from the transient response of terminal voltage by executing the PCD profile as a battery characterisation test at room temperature [27]. The Turnigy LiPB in Fig. 3 is used in the experiments. It comprises of a LiMn$_2$O$_4$ cathode and an artificial graphite anode, which are usually laminated with the solid electrolyte and the separator sheets and enclosed in a foil-type case. The solid electrolyte enables batteries safer and allows the use of higher energy electrode materials designed for high power applications. The LiPB has a nominal capacity of 5.0 Ah and a nominal voltage of 3.7 V. The dimension of the cell is 135 mm × 50 mm × 9 mm and the weight of the cell is 130 g. A battery testing platform as illustrated in Fig. 4 is developed to conduct experiments, which consists of a host computer, a programmable power supply (Sorensen DLM50-60), an electronic load (Prodigit 3320) and a safety control switch box. The battery testing platform can control charge/discharge battery current, sample battery terminal voltage current and temperature, and then record the data into the computer via a graphic user interface program designed by using the LABVIEW software.

The PCD profile as an off-line method was performed for the BECM parameters identification as shown in Fig. 5. Initially, the LiPB was fully charged (SOC = 100%) at room temperature, and left it in the open circuit state for an hour so that the OCV is able to reach its equilibrium state. Then, the LiPB was discharged by a sequence of 5.0 A pulse currents consisting of 6-min discharge and 1 h rest between two consecutive pulse currents to allow the OCV return to the equilibrium state. Each pulse current discharges approximately 10% of the nominal capacity, which is equivalent to 10% of the SOC reduction. The procedure of the pulse current discharge and recovery was iterated until the terminal voltage reached the cut-off voltage of 2.7 V as the battery fully discharged state (SOC = 0%). The corresponding voltage response is shown in Fig. 5. It can be seen that totally ten sets of transient response in terminal voltage generated to determine circuit parameters for ten different SOCs. Meanwhile, with the aid of Ah counting method, the nonlinear relationship between the OCV and the SOC over entire operation range can be obtained by conducting the PCD profile on the LiPB and the corresponding nonlinear curve as shown in Fig. 2.

Intuitively, during relaxation period each terminal voltage can be represented by

$$V_t(t) = V_{oc} - V_{pe} \exp(-t/\tau_{pe}) - V_{pc} \exp(-t/\tau_{pc}) \tag{16}$$
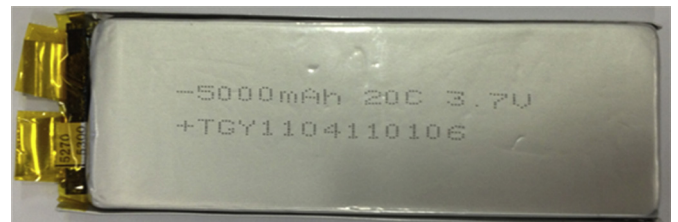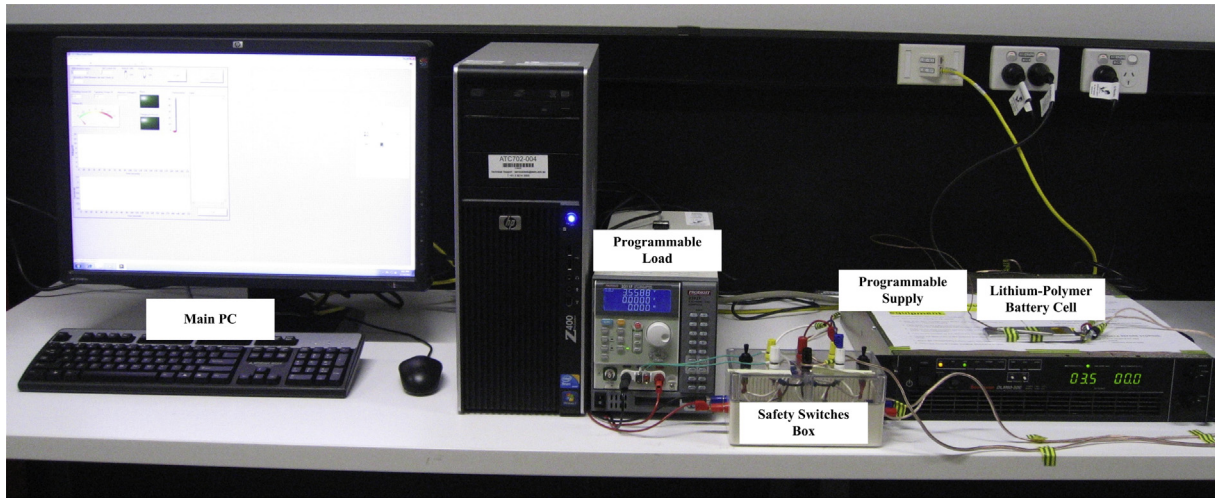

Fig. 3. Photo of Turnigy LiPB.

Fig. 4. Testing platform for the LiPB.

where τ_{pe} and τ_{pc} are the time constants for the electrochemical polarisation and concentration polarisation voltages during transient response, respectively. V_{oc} is the OCV after a full relaxation. V_{pe} and V_{pc} are the voltages of the electrochemical and concentration polarisation capacitors, respectively. According to the circuit analysis, the following equations are derived to calculate the parameters

$$R_{pe} = V_{pe}/I \qquad (17)$$

$$R_{pc} = V_{pc}/I \qquad (18)$$

$$C_{pe} = \tau_{pe}/R_{pe} \qquad (19)$$

$$C_{pc} = \tau_{pc}/R_{pc} \qquad (20)$$

The ohmic resistance is given by

$$R_{in} = \Delta V_t/I \qquad (21)$$

As an example, the transient response of terminal voltage at the second pulse current indicated by a red circle in Fig. 5 was used to extract the circuit parameters, where the circled section is magnified in Fig. 6. With the circuit parameters identified by using a curve fitting technique based on Eq. (16) and calculated by Eqs. (17)–(21), the curve fitting results are plotted in Fig. 6 in the red dash line.

The pulse current discharge was repeated ten times corresponding to different SOCs, thus ten groups of circuit parameters were obtained and summarised in Table 1 with the curve fitting errors represented by root mean square errors (RMSEs). The BECM has a small deviation from the LiPB in the training profile due to
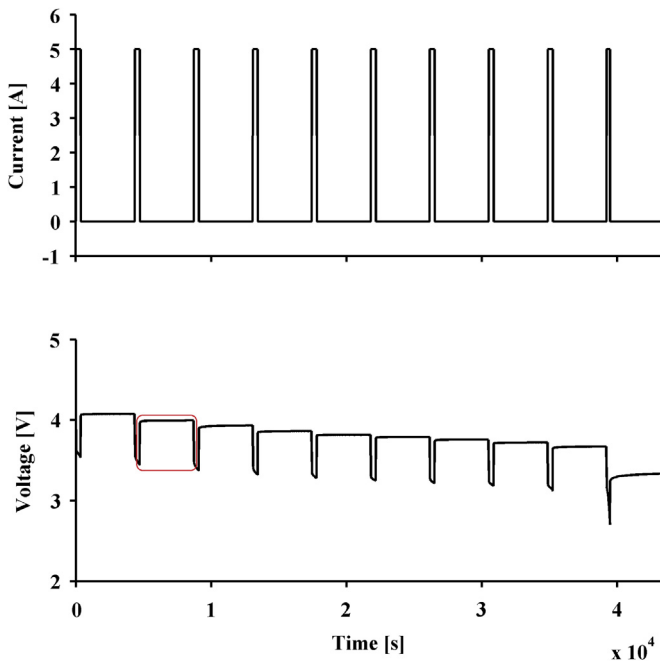

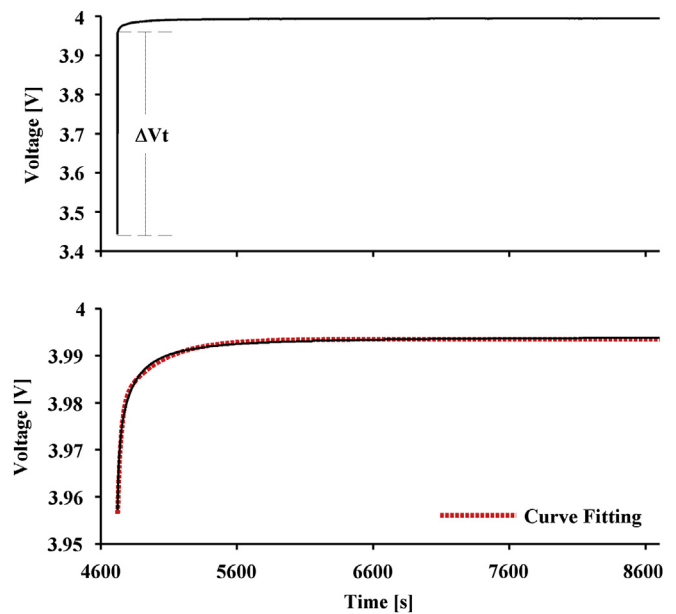**Fig. 5.** Pulse current discharges and corresponding terminal voltages.

Fig. 6. Transient response of the LiPB and BECM for second pulse current.

Table 1
Circuit parameters of BECM and RMSEs at different SOCs.

SOC	R_{in} (mΩ)	R_{pe} (mΩ)	C_{pe} (kF)	R_{pc} (mΩ)	C_{pc} (kF)	RMSE
90%	102.1	4.62	4.05	1.34	12.26	0.0256
80%	102.5	4.96	4.93	2.86	14.33	0.0293
70%	102.9	4.23	7.05	4.92	16.67	0.0268
60%	103.0	3.58	5.51	2.17	17.52	0.0238
50%	102.9	3.62	4.81	1.19	12.98	0.0266
40%	103.1	4.12	6.03	1.45	13.94	0.0272
30%	103.2	3.36	6.62	1.63	16.46	0.0285
20%	103.3	3.16	6.02	1.52	18.71	0.0245
10%	103.3	4.13	6.95	3.27	20.54	0.0274
0%	104.6	10.31	6.76	12.23	21.387	0.0289

non-zero RMSEs. Since the parameters at 80% of SOC caused the largest fitting error as listed in Table 1, they were used to calculate the system parameters in Eq. (8).

To illustrate the modelling errors caused by using constant circuit parameters and demonstrate the robustness of the ASGSMO in presence of the modelling errors, the constant current discharge (CCD), city and suburban current profiles are concurrently loaded to the LiPB and the BECM, where the city and suburban current profiles simulate more realistic EV driving conditions in both city and suburban, respectively [31]. These profiles with the average discharge current of $1/3C_n$, $1C_n$ and $1.5C_n$ are adopted to conduct experiment in this paper, which are corresponding to normal EV driving conditions. As an example, three profiles with the average discharging rate $1C_n$ and their experimental results in terms of battery and the estimated voltages from the BECM are shown in Figs. 7–9, respectively. It can be seen that the BECM output voltages are not able to track the LiPB voltage and there always exists modelling errors in each profile and their RMSEs associated with various discharging rates are listed in Table 2. It shows that modelling errors are increased in large discharge current rates and the model accuracies are relatively low in such conditions due to the fixed model parameters obtained from the off-line identification. To overcome the model inaccuracy issue, the ASGSMO will be designed to provide the robust SOC estimation by compensating the modelling errors and uncertainties in the next section.
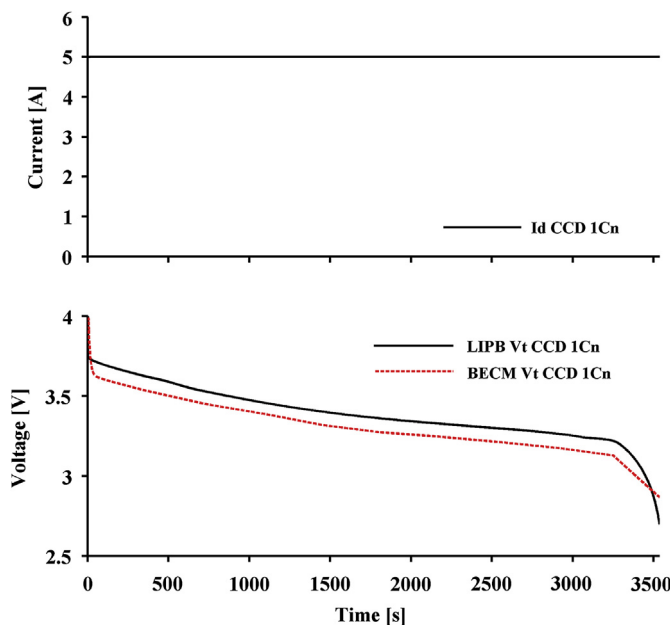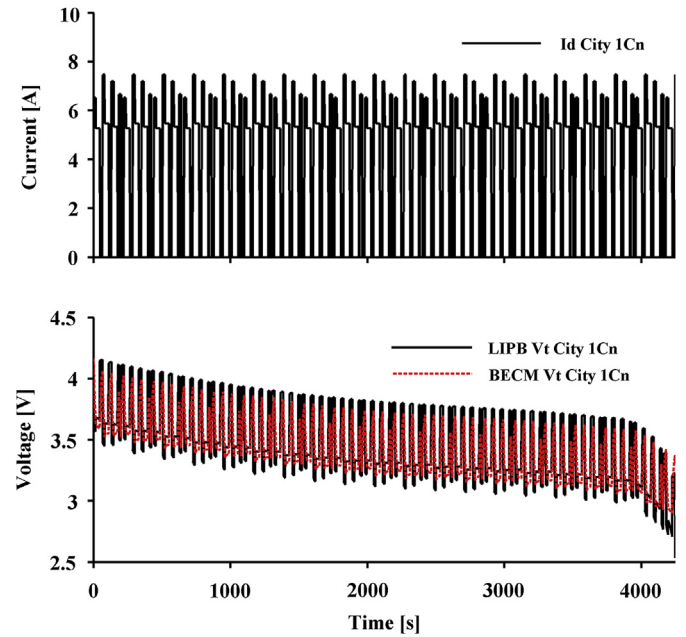

Fig. 8. City $1C_n$ profile and terminal voltages of LiPB and BECM.

3. Design of adaptive switching gain sliding mode observer for SOC estimation

The SMOs with constant switching gains for the SOC estimation have demonstrated the robustness to modelling errors and disturbances with properly chosen switching gains [26,27]. Since the modelling errors and the SOC estimation errors are closely related to battery discharge current profiles, which vary between $1/3C_n$ and $1.5C_n$ discharge rates averagely corresponding to normal EV driving conditions, the robust and accurate SOC estimation is unlikely to be achieved by using SMOs with un-adjustable switching gains for various discharge current rates. Either underestimated or
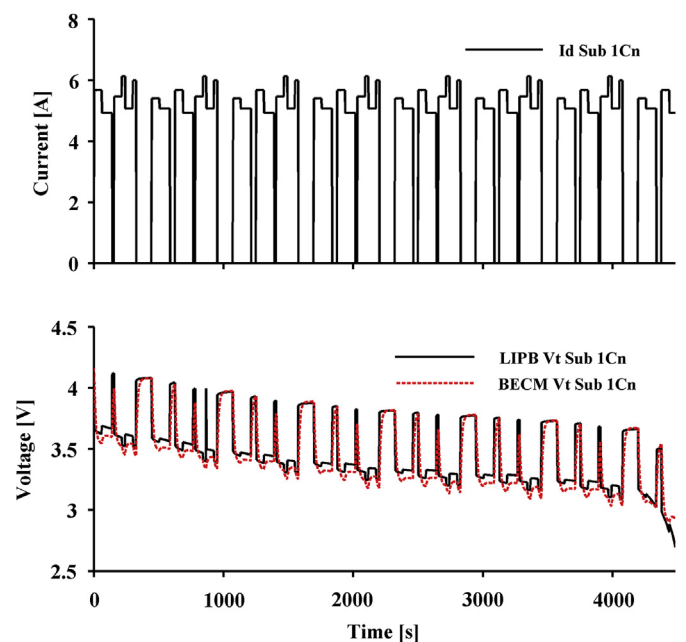

Fig. 7. CCD $1C_n$ profile and terminal voltages of LiPB and BECM.

Fig. 9. Suburban $1C_n$ and terminal voltages of LiPB and BECM.

Table 2
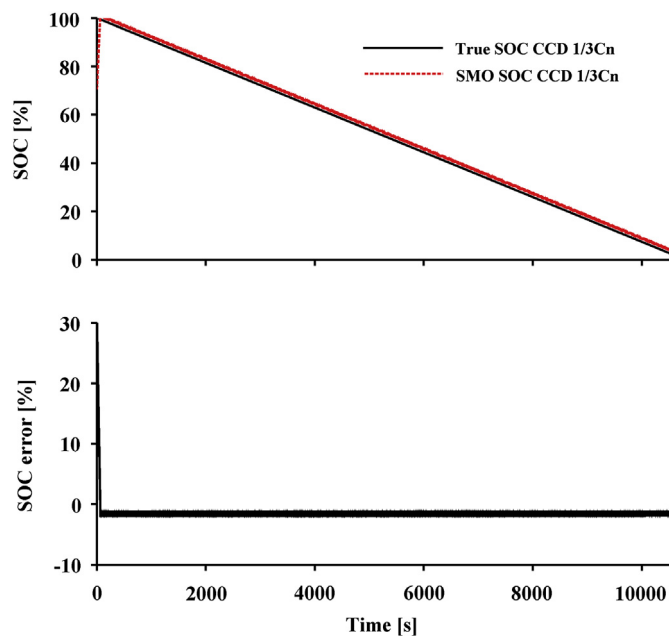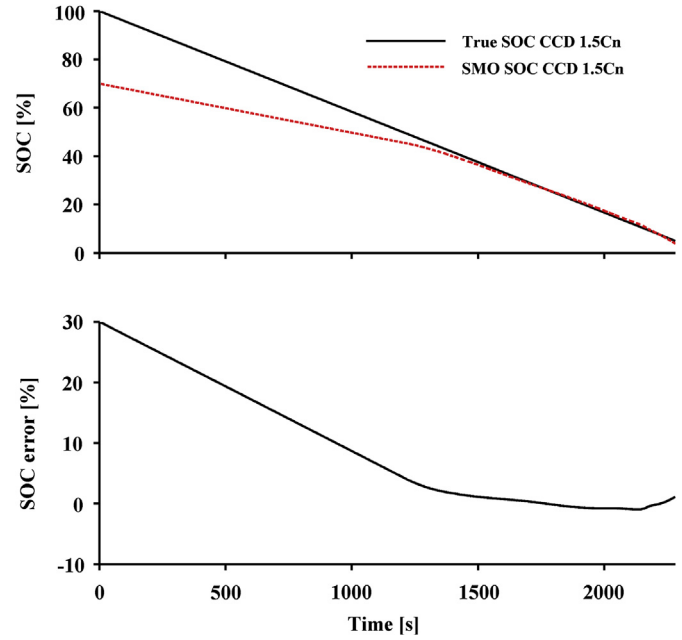Modelling errors of BECM expressed as RMSEs in CCD/city/suburban profiles.

Current profile	RMSE of BECM
CCD 1.5C_n	0.164
CCD 1C_n	0.128
CCD 1/3C_n	0.096
City 1.5C_n	0.284
City 1C_n	0.238
City 1/3C_n	0.193
Suburban 1.5C_n	0.185
Suburban 1C_n	0.137
Suburban 1/3C_n	0.105

overestimated switching gains can lead to the poor tracking performance or the undesired chattering phenomena in the SOC estimation results, respectively.

For instance, the ordinary SMO with conservative switching gains is able to estimate the SOC with low magnitude of chattering in 1/3C_n CCD profile as shown in Fig. 10, but its tracking performance under 1.5C_n CCD profile is very poor with average SOC estimation error more than 10% as shown in Fig. 11. On the other hand, the tracking performance of the SMO with large switching gains is significantly improved for 1.5C_n CCD profile with most of estimation errors bounded within 3% as shown in Fig. 12, but it produces high magnitudes of chattering phenomena for the SOC estimation in 1/3C_n CCD profile as shown in Fig. 13, and significant chattering effect can result in instability of observer and the blurred SOC estimation results. In other words, the SOC estimation error would be large or divergent if the inappropriate switching gains were used in the highly dynamic current profile.

Therefore, in order to accurately estimate the SOC for various discharge current profiles, the ASGSMO based on the BECM is proposed as follows

$$\dot{\hat{x}}(t) = A\hat{x}(t) + Bu(t) + K(y(t) - C\hat{x}(t)) + v \tag{22}$$

Fig. 11. Ordinary SMO-based SOC estimation with conservative switching gains for CCD 1.5C_n.

$$\hat{y}(t) = C\hat{x}(t) \tag{23}$$

where the feedback gain matrix, K and the adaptive switching gains function, v can be designed so that the stability and robustness of the ASGSMO is guaranteed.

$$v = \begin{cases} \hat{\theta}(e_y(t)) \Gamma \mathrm{sgn}\,(e_y(t)) & \text{if } e_y(t) \neq 0 \\ 0 & \text{otherwise} \end{cases} \tag{24}$$

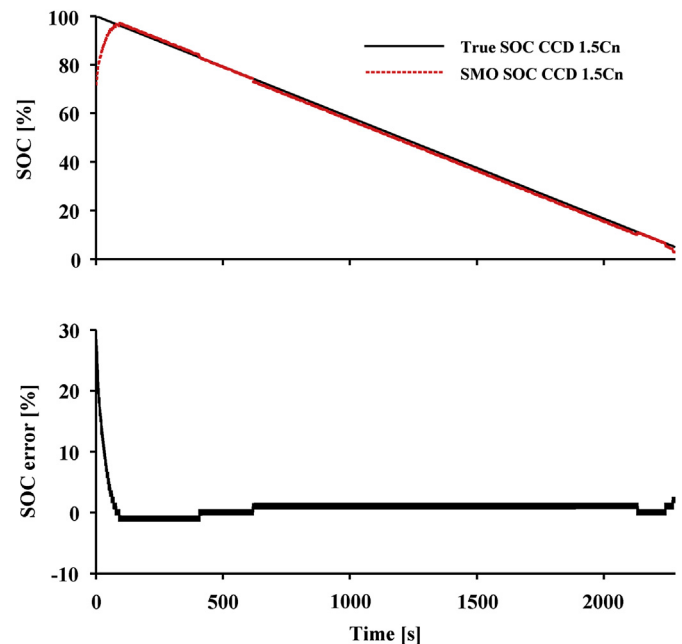The discontinuous switching term is defined as

Fig. 10. Ordinary SMO-based SOC estimation with conservative switching gains for CCD 1/3C_n.

Fig. 12. Ordinary SMO-based SOC estimation with large switching gains for CCD 1.5C_n.
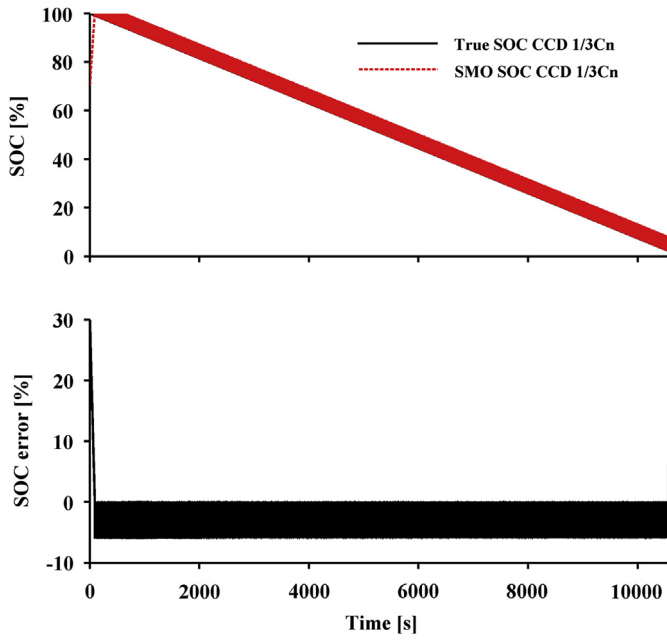
Fig. 13. Ordinary SMO-based SOC estimation with large switching gains for CCD 1/3C_n.

$$\text{sgn}\left(e_y(t)\right) = \begin{cases} +1, & e_y(t) > 0 \\ -1, & e_y(t) < 0 \end{cases} \tag{25}$$

where $e_y(t) = y(t) - \widehat{y}(t) = Ce(t)$ and the adaptive switching gain $\widehat{\theta}(Ce(t))$ are updated by the following adaptive law

$$\dot{\widehat{\theta}}\left(e_y(t)\right) = \alpha|e_y(t)| \tag{26}$$

where α is a positive constant, which can be chosen to adjust the speed adaptation for switching gains function.

The state estimation errors are defined as $e(t) = x(t) - \widehat{x}(t)$ and subtracting Eq. (22) from Eq. (13) gives the dynamical state estimation error system as

$$\dot{e}(t) = A_0 e(t) + \Gamma \xi(x, t) - v \tag{27}$$

where $A_0 = (A - KC)$.

According to the Remark 2, there exists a system feedback gain matrix K such that $A_0 = A - KC$ is a strictly Hurwitz matrix, where K can be directly obtained by using either the pole placement method or linear quadratic regulator (LQR) method.

Based on an appropriate Lyapunov equation (LE), there exists a symmetric definite matrix P as the solution of the LE

$$A_0 P + P A_0^T = -Q \tag{28}$$

where Q is a symmetric positive definite matrix such that the structural constraint

$$C = \Gamma^T P \tag{29}$$

is satisfied by a Lyapunov matrices pair (P, Q) for A_0.

It can be seen from Eq. (27) that if the adaptive switching gains function v is properly adjusted corresponding to the state estimation errors so that the asymptotically stability of the reconstruction error system is guaranteed if Eq. (29) is fullfied. Thus, a sliding mode motion can be induced on the system error states and the state estimation errors is asymptotically converged to zeros as time

tends to infinity, a Lyapunov function candidate including both state errors and adaptive error is considered as follows

$$V\left(e(t), \tilde{\theta}(t)\right) = (1/2)\left(e^T P e + \alpha^{-1}\tilde{\theta}^2\right) \tag{30}$$

where $\tilde{\theta}(t) = \widehat{\theta}(t) - \theta_d$ is the adaptation error between estimated switching gain and desired switching gain. Taking the time derivative of the candidate of Lyapunov function V gives

$$\begin{aligned} \dot{V} &= (1/2)\left(\dot{e}^T P e + e^T P \dot{e}\right) + \alpha^{-1}\tilde{\theta}\dot{\tilde{\theta}} \\ &= (1/2)\left[e^T\left(A_0 P + P A_0^T\right)e\right] + (1/2)\left\{\left[\xi^T \Gamma^T - v^T\right]P e \right. \\ &\quad \left. + e^T P[\Gamma\xi - v]\right\} + \alpha^{-1}\tilde{\theta}\dot{\tilde{\theta}} \\ &= -(1/2)e^T Q e + \xi\Gamma^T P e - v^T P e + \alpha^{-1}\left[\widehat{\theta}(t) - \theta_d\right]\dot{\tilde{\theta}} \\ &= -(1/2)e^T Q e + \xi C e - \widehat{\theta}(t)\text{sgn}\left(e_y\right)\Gamma^T P e + \alpha^{-1}\left[\widehat{\theta}(t) - \theta_d\right] \\ &\quad \times \left(\alpha|e_y(t)|\right) \\ &= -(1/2)e^T Q e + \xi e_y - \widehat{\theta}(t)|e_y(t)| + \left[\widehat{\theta}(t) - \theta_d\right]|e_y(t)| \\ &= -(1/2)e^T Q e + [\xi - \theta_d\text{sgn}\left(e_y\right)]e_y \end{aligned}$$
$$\tag{31}$$

The term $-(1/2)e^T Q e$ is always negative and the resultant equation will be $\dot{V} < 0$ as

$$\begin{aligned} &[\xi - \theta_d\text{sgn}\left(e_y\right)]e_y < 0 \text{ for } e_y > 0 \text{ if } \theta_d > \psi \\ &[\xi - \theta_d\text{sgn}\left(e_y\right)]e_y < 0 \text{ for } e_y < 0 \text{ if } \theta_d > \psi \end{aligned} \tag{32}$$

As $|\xi(x,t)| \leq \psi$ and there exists a desired finite non-negative switching gain θ_d such that $\theta_d > \psi$, leading to $\dot{V} < 0$, which satisfies the second method of Lyapunov stability theory. Therefore, the state estimation error system Eq. (27) asymptotically converges to zero as time tends to infinity. Once the sliding surface is reached, the influence of the bounded model uncertainty $\xi(x, t)$ is compensated and the asymptotic stability of the ASGSMO is guaranteed. As the switching gains are adaptively updated in response to the dynamics of system state errors, the ASGSMO can provide robust tracking capability against modelling errors and significantly reduce the magnitude of chattering in the SOC estimation. The next section will present the experimental results to validate the proposed method for the effectiveness in SOC estimation.

4. Verification of ASGSMO for SOC estimation

The configuration of the ASGSMO for the SOC estimation is illustrated in Fig. 14, where the properly defined discharge current profiles are simultaneously applied to the LiPB integrated with Ah counting module and the ASGSMO module. The LiPB terminal voltage is sampled and fed into the ASGSMO to generate the output tracking error, which can be used to update the corresponding switching gains of ASGSMO so as to compensate the modelling errors. The resultant output of ASGSMO module is the estimated SOC, which is concurrently compared to the true SOC directly generated by an Ah counting module to show the accuracy of the SOC estimation.

The feedback gain matrix, K is obtained by using the LQR method with Riccati equation as

$$K = [1.4244 \quad 1.4062 \quad -0.1451 \quad -0.2950]^T \tag{33}$$

The matched model uncertainties are determined by the largest modelling errors after comparing experimental LiPB data with
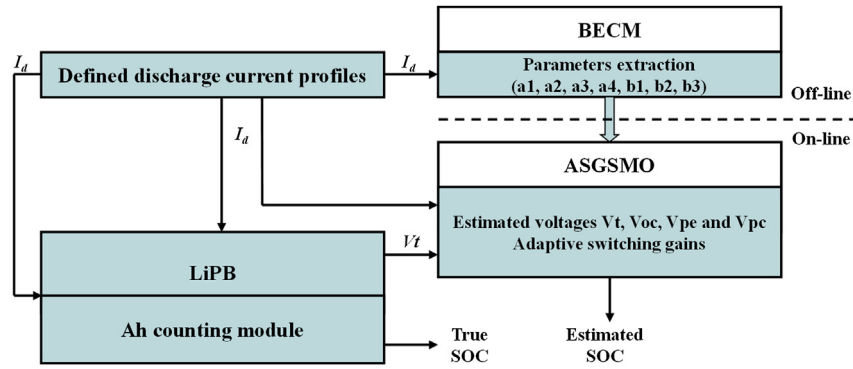
Fig. 14. Configuration of proposed ASGSMO system.

model data so that the bound of model uncertainties satisfy $|\xi(x,t)| \leq 0.2$. The model uncertainties input matrix, Γ is defined as

$$\Gamma = [1.4516 \quad -0.0326 \quad 0.0122 \quad 0.0204]^T \qquad (34)$$

And according to an algorithm for the design of P [32], let $Q = 2I_4$, the symmetric positive definite matrix P of the LE (22) can be determined as
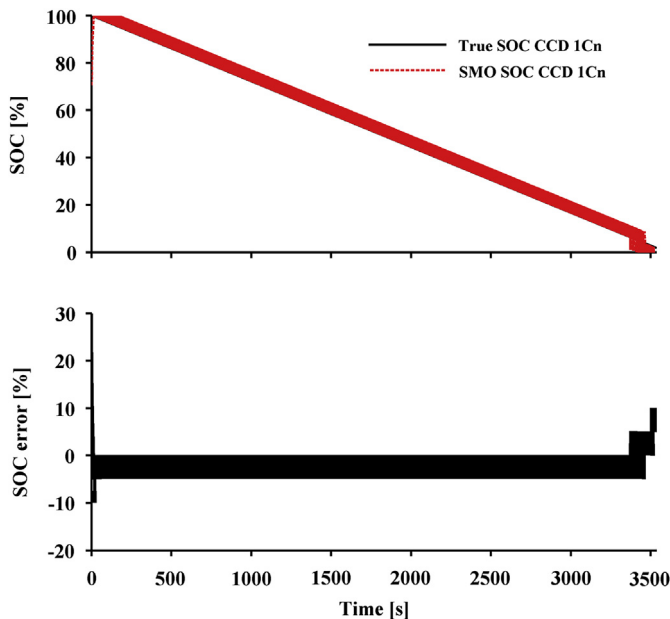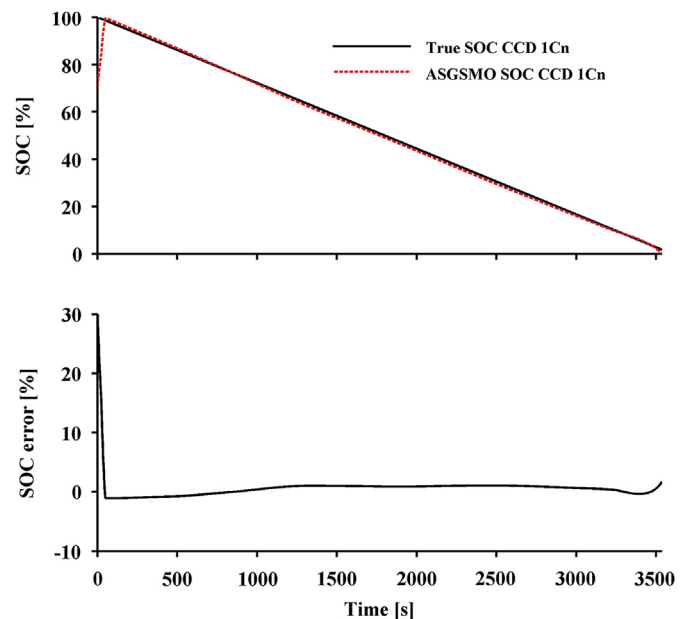
$$P = \begin{bmatrix} 0.7075 & 0.7032 & -0.0746 & -0.1500 \\ 0.7032 & 44.2880 & 5.2992 & 17.6076 \\ -0.0746 & 5.2992 & 24.1883 & -0.6702 \\ -0.1500 & -6.2178 & -0.6702 & 39.1701 \end{bmatrix} \qquad (35)$$

The positive constant, α is selected as 0.5 to satisfy the adaptation speed for the switching gains function. To validate the effectiveness and robustness of the ASGSMO for the SOC estimation, three types of discharge current profile with various discharge rates have been conducted on the LiPB at the approximately room temperature of 25 °C. As the battery is fully charged, the initial SOC of the LiPB is set to 100% before loading each discharge current profile.

In order to demonstrate the better performance of the ASGSMO over the conventional SMO for the SOC estimation, three current profiles as shown in Figs. 7–9 with average discharge currents of 1/

$3C_n$, $1C_n$ and $1.5C_n$ have been used to conduct experiment on the testing platform.

The first set of testing data is obtained by using the CCD profile with discharge rates of $1/3C_n$, $1C_n$ and $1.5C_n$, namely 1.67 A, 5 A, and 7.5 A. The ordinary SMO and the proposed ASGSMO are used to estimate at any initial SOC (e.g. 70%) for different discharge current rates. As an example, the results of the CCD with $1C_n$ rate are shown in Figs. 15 and 16, respectively. It can be found that both methods are robust to incorrect initial SOCs. With relatively large constant switching gains, the conventional SMO even achieves faster SOC estimation convergence, but the significant chattering ripples are observed on the SOC estimation results due to its inability of adaptively updating the switching gains. Fig. 15 shows its estimation errors which are bounded in ±10%. Comparing with the SMO, the ASGSMO can track the true SOC with reasonable convergence speed and small chattering ripples, its SOC tracking errors are fluctuating in the small range of −2% to +2%, as shown in Fig. 16. This is due to the fact that the switching gains of the ASGSMO can be adaptively tuned to the proper low levels as the corresponding estimation errors decrease. To further show the robustness of the proposed ASGSMO for different initial SOCs, Fig. 17 shows the RMSE of the SOC estimation errors for the initial SOCs from 0% to 100% in the step of 10%, they are all within 3%.

Fig. 15. Ordinary SMO-based SOC estimation for CCD $1C_n$.

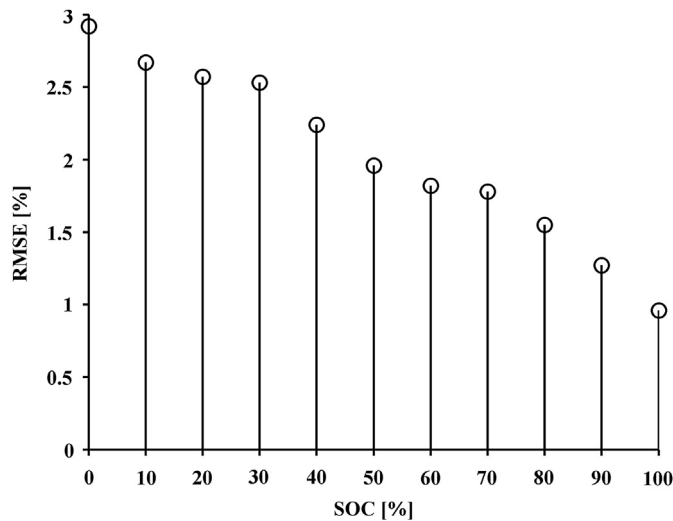**Fig. 16.** ASGSMO-based SOC estimation errors for CCD $1C_n$.

Fig. 17. RMSEs of ASGSMO-based SOC estimation at different initial SOCs for CCD $1C_n$.

The second and third sets of testing data are obtained from city and suburban current profiles which emulate the typical driving cycles as a driver commuting between home and work in both city and suburban settings [31]. Both city and suburban current profiles are performed with average discharging rates of $1/3C_n$, $1C_n$ and $1.5C_n$. As an example, the SOC estimation results of two observers in city current profile with average $1C_n$ rate are shown in Figs. 18 and 19, respectively. The city current profile as given in Fig. 8 characterises the congested traffic conditions in city with repetitive cycles of acceleration and braking. The initial SOC is also set to 70%. For the SMO-based approach, Fig. 18 illustrates the SOC estimation results and the estimation errors which are bounded in $\pm10\%$ with significant chattering ripples. For the ASGSMO-based approach, the SOC estimation errors are reduced to the range of $+3\%$ and -3% for 10–90% of SOC with minor chattering ripples, as shown in Fig. 19. Meanwhile, the ASGSMO has performed superior robustness and
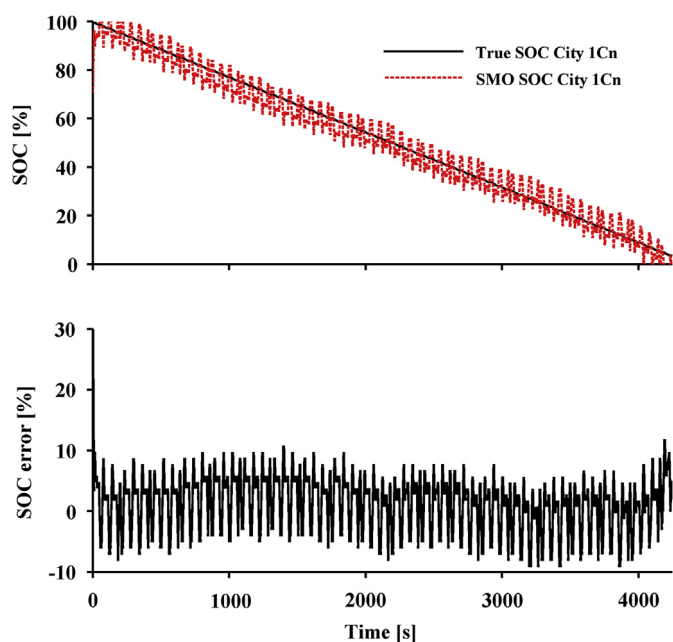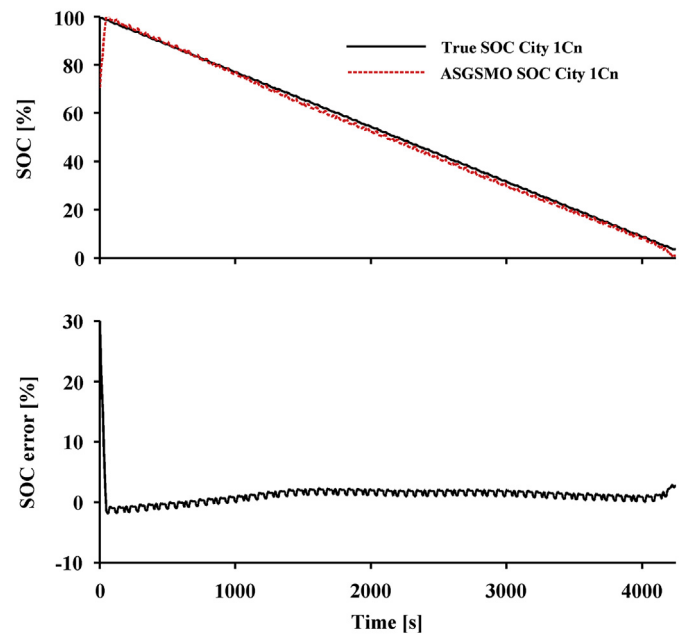

Fig. 19. ASGSMO-based SOC estimation errors for city $1C_n$.

capability to track the true SOC regardless of incorrect initial SOCs with all the RMSEs within 4%, as shown in Fig. 20. As another example, the SOC estimation results of both SMO-based and ASGSMO-based methods in suburban current profile with average $1C_n$ rate are shown in Figs. 21 and 22, respectively. This profile characterises the smooth driving conditions in suburban with minimal stops. With the same initial SOC of 70% as the city profile, the SMO-based approach gives the SOC estimation errors within $\pm10\%$ as shown in Fig. 21 while the ASGSMO-based approach gives the SOC estimation errors in the range of $+3\%$ and -3% for 10–90% of SOCs with nearly smooth SOC estimation results as shown in Fig. 22. The RMSEs of the SOC estimation for different initial SOCs varying from 0% to 100% in the step of 10% are all less than 3.5%, as shown in Fig. 23. Table 3 summarises the RMSEs of the SOC estimation for each type of current profile with average different discharge rates. It can be seen that the RMSEs of the SOC estimation
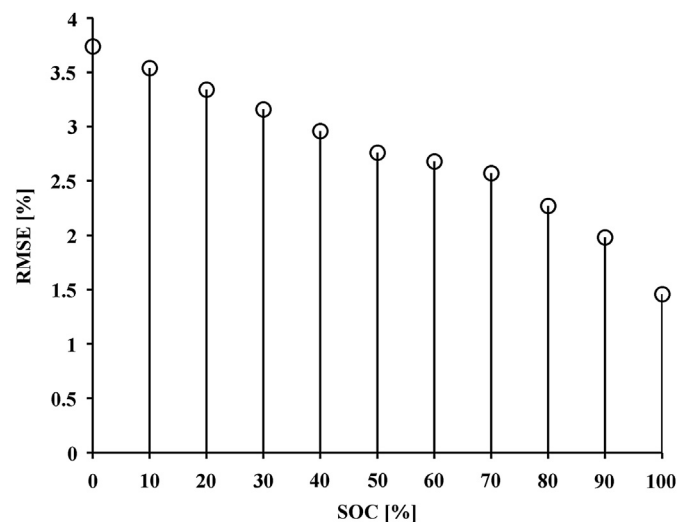

Fig. 18. Ordinary SMO-based SOC estimation for city $1C_n$.

Fig. 20. RMSEs of ASGSMO-based SOC estimation at different initial SOCs for city $1C_n$.

Fig. 21. Ordinary SMO-based SOC estimation for suburban $1C_n$.

Fig. 23. RMSEs of ASGSMO-based SOC estimation at different initial SOCs for suburban $1C_n$.
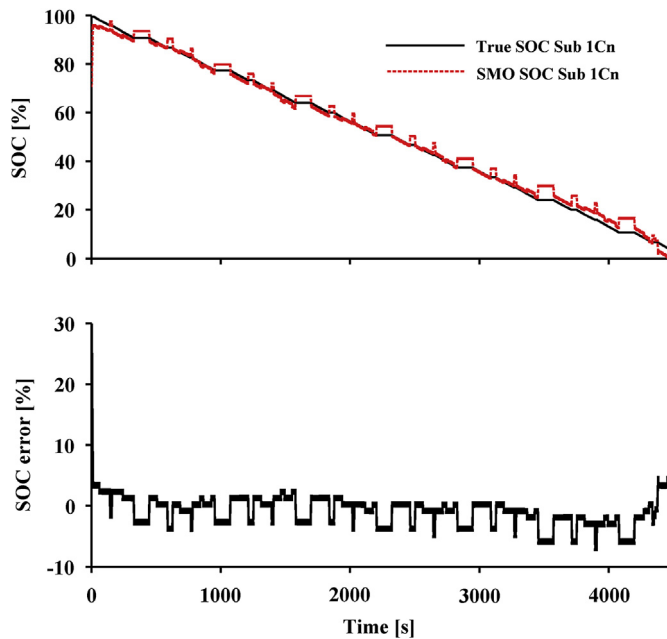
based on the ASGSMO is always lower than those based on the conventional SMO.

To further illustrate the improved accuracy of the SOC estimation, the probability of relative SOC estimation errors bounded in 5% for both the SMO and the ASGSMO under the above-mentioned three different current profiles has been evaluated and summarised in Table 4. It can be seen that the ASGSMO has performed better SOC estimation with approximately 99% of estimation errors bounded in 5% than the SMO with only approximately 83%. Therefore, the proposed ASGSMO can provide more robust and accurate SOC estimation with less chattering effects than the conventional SMO.
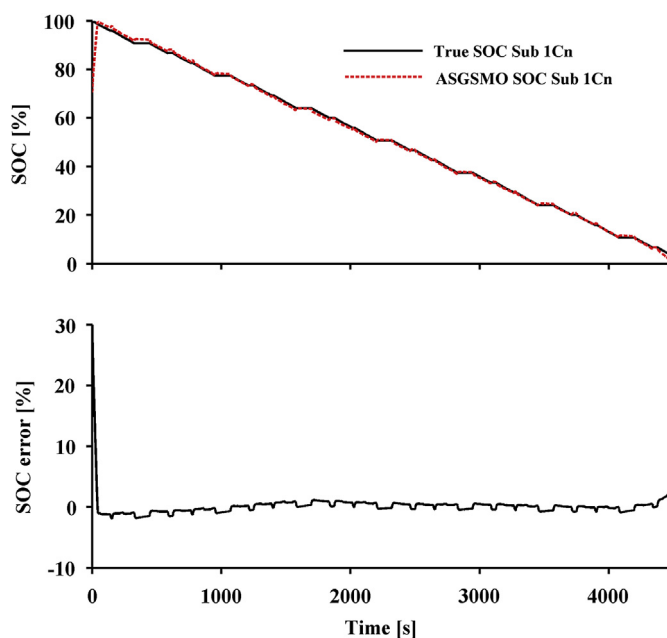
Table 3
Comparison of SOC estimation RMSEs based on SMO and ASGSMO in CCD/city/suburban profiles.

Current profile	SMO SOC estimation RMSE	AGSMO SOC estimation RMSE
CCD $1.5C_n$	0.166	0.026
CCD $1C_n$	0.154	0.018
CCD $1/3C_n$	0.092	0.013
City $1.5C_n$	0.247	0.031
City $1C_n$	0.192	0.026
City $1/3C_n$	0.143	0.017
Suburban $1.5C_n$	0.233	0.029
Suburban $1C_n$	0.184	0.022
Suburban $1/3C_n$	0.132	0.013

5. Conclusions

The adaptive switching gain sliding mode observer (ASGSMO) based on the BECM has been presented to estimate battery SOC in EVs and it is able to compensate modelling errors caused by the parameter variations of the BECM. The LiPB is utilised to conduct the experiments. The parameters of the BECM are extracted from the experimental data under a sequence of pulse current discharge. The performance and effectiveness of the SOC estimation based on the proposed ASGSMO have been verified by the experimental results of a LiPB under different discharge rates of various current

Fig. 22. ASGSMO-based SOC estimation errors for suburban $1C_n$.

Table 4
Comparison of probability of relative SOC estimation errors bounded in 5% based on SMO and ASGSMO in CCD/city/suburban profiles.

Current profile	Probability of SMO SOC estimation error bounded in 5% (%)	Probability of ASGSMO SOC estimation error bounded in 5% (%)
CCD $1.5C_n$	79.36	98.73
CCD $1C_n$	85.52	98.95
CCD $1/3C_n$	88.47	99.21
City $1.5C_n$	71.28	98.76
City $1C_n$	76.34	99.17
City $1/3C_n$	80.82	99.32
Suburban $1.5C_n$	77.76	98.87
Suburban $1C_n$	81.92	99.24
Suburban $1/3C_n$	84.29	99.65

profiles. It shows that the proposed ASGSMO has a robust tracking capability in the SOC estimation with less chattering levels and high estimation accuracy in the comparison of the conventional SMO.

Acknowledgment

References

[1] K.E. Aifantis, S.A. Hackney, R.V. Kumar, High Energy Density Lithium Batteries, Materials, Engineering, Applications, Wiley-VCH Verlag GmbH & Co. KGaA, Weinheim, 2010.
[2] T.B. Reddy, Linden's Handbook of Batteries, fourth ed., McGraw Hall, 2010.
[3] S. Piller, M. Perrin, A. Jossen, Journal of Power Sources 96 (1) (2001) 113–120.
[4] V. Pop, H.J. Bergveld, P.H.L. Notten, P.P.L. Regtien, Journal of Measurement Science and Technology 16 (12) (2005) 93–110.
[5] L. Lu, X. Han, J. Li, J. Hua, M. Ouyang, Journal of Power Sources 226 (3) (2013) 272–288.
[6] K.S. Ng, C.-S. Moo, Y.-P. Chen, Y.-C. Hsieh, Journal of Applied Energy 86 (9) (2009) 1506–1511.
[7] S. Rodrigues, N. Munichandraiah, A.K. Shukla, Journal of Power Sources 87 (4) (2000) 12–20.
[8] H. Blanke, O. Bohlen, S. Buller, R.D. Doncker, B. Fricke, A. Hammouche, D. Linzen, M. Thele, D.U. Sauer, Journal of Power Sources 144 (6) (2005) 418–425.
[9] J.L. Jespersen, A.E. Tonnesen, K. Norregaard, L. Overgaard, F. Elefsen, World Electric Vehicle Journal 3 (5) (2009) 2032–6653.
[10] C.C. Chan, E.W.C. Lo, W.X. Shen, Journal of Power Sources 87 (11) (2000) 201–204.
[11] W.X. Shen, C.C. Chan, E.W.C. Lo, K.T. Chau, Journal of Energy Conversion Management 43 (4) (2002) 817–826.
[12] W.X. Shen, C.C. Chan, E.W.C. Lo, K.T. Chau, IEEE Transactions on Industrial Electronics 49 (7) (2002) 677–684.
[13] T. Hansen, C.-J. Wang, Journal of Power Sources 141 (3) (2005) 351–358.
[14] O. Barbarisi, F. Vasca, L. Glielmo, Journal of Control Engineering Practice 14 (3) (2006) 267–275.
[15] J. Wang, B. Cao, Q. Chen, F. Wang, Journal of Control Engineering Practice 15 (5) (2007) 1569–1576.
[16] A. Vasebi, M. Partovibakhsh, S. Mohammed, Journal of Power Sources 17 (11) (2007) 30–40.
[17] B.S. Bhangu, P. Benley, D.A. Stone, C.M. Bingham, IEEE Transactions on Vehicular Technology 54 (3) (2005) 783–794.
[18] G. Plett, Journal of Power Sources 161 (10) (2006) 1356–1368.
[19] G. Plett, Journal of Power Sources 161 (10) (2006) 1369–1384.
[20] J. Zhang, C. Xia, Journal of Electrical Power & Energy Systems 33 (3) (2011) 472–476.
[21] W. He, N. Williard, C. Chen, M. Pecht, Journal of Microelectronics Reliability 53 (6) (2013) 840–847.
[22] J. Han, D. Kim, M. Sunwoo, Journal of Power Sources 188 (3) (2009) 606–612.
[23] F. Sun, X. Hu, Y. Zou, S. Li, Energy 36 (5) (2011) 3531–3540.
[24] F. Zhang, G. Liu, L. Fang, H. Wang, IEEE Transactions on Industrial Electronics 59 (2) (2012) 1086–1095.
[25] J. Yan, G. Xu, H. Qian, Y. Xu, Energies 3 (10) (2010) 1654–1672.
[26] I. Kim, Journal of Power Sources 163 (10) (2006) 584–590.
[27] X.P. Chen, W.X. Shen, Z.W. Cao, A. Kapoor, Australian Journal of Electrical & Electronics Engineering 9 (3) (2012) 225–234.
[28] M. Chen, A. Gabriel, M. Rincon, IEEE Transactions on Energy Conversion 21 (2) (2006) 504–511.
[29] H. He, R. Xiong, J. Fan, Energies 4 (3) (2011) 582–598.
[30] X. Hu, S. Li, H. Peng, Journal of Power Sources 198 (10) (2012) 359–367.
[31] E. Martinez-Rosas, R. Vasquez-Medrano, A. Flores-Tlacuahuac, Journal of Computers and Chemical Engineering 35 (5) (2011) 1937–1948.
[32] C. Edwards, S. Spurgeon, International Journal of Control 59 (5) (1994) 1211–1229.

Glossary

A, B, C: system parameters matrices
C_n: nominal capacity of LiPB (Ah)
C_{pe}: electrochemical polarisation capacitance (F)
C_{pc}: concentration polarisation capacitance (F)
$e(t)$: state estimation error
$e_y(t)$: output estimation error
K: system feedback gain matrix
R_{in}: ohmic resistance (Ω)
R_{pe}: electrochemical polarisation resistance (Ω)
R_{pc}: concentration polarisation resistance (Ω)
Soc: state of charge
$\hat{Soc}$: estimated state of charge
V_{oc}: open circuit voltage (V)
$V_{oc}(Soc)$: open circuit voltage as a function of state of charge
V_{pe}: electrochemical polarisation voltage (V)
$\hat{V}_{pe}$: estimated electrochemical polarisation voltage (V)
V_{pc}: concentration polarisation voltage (V)
$\hat{V}_{pc}$: estimated concentration polarisation voltage (V)
$\hat{V}_t$: estimated battery terminal voltage (V)
V_t: battery terminal voltage (V)
$x(t)$: system states
$y(t)$: system output state
α: adaptive law parameter
η: Coulombic efficiency
$\Delta V_{oc}, \Delta R_{in}, \Delta R_{pe}, \Delta C_{pe}, \Delta R_{pc}, \Delta C_{pc}$: variations of circuit parameters
$\Delta f_1, \Delta f_2, \Delta f_3, \Delta f_4$: model uncertainties
Γ: system uncertainties input matrix
$\lambda_1, \lambda_2, \lambda_3, \lambda_4$: eigenvalues of system matrix, A
ξ: matched uncertainty function
ψ: matched uncertainty bound
υ: adaptive switching gains function